12th International Symposium on Turbulence and Shear Flow Phenomena (TSFP12)
Osaka, Japan (Online), July 19-22, 2022

# SMALL-SCALE DENSITY FLUCTUATIONS IN GRID-GENERATED TURBULENCE IN A SALT-STRATIFIED FLUID

**Shinya Okino**
Department of Mechanical Engineering and Science
Kyoto University
Kyoto daigaku-katsura 4, Nishikyo-ku, Kyoto 615-8540, Japan
okino.shinya.8n@kyoto-u.ac.jp

**Soichiro Minakami**
Department of Mechanical Engineering and Science
Kyoto University
Kyoto daigaku-katsura 4, Nishikyo-ku, Kyoto 615-8540, Japan
minakami.soichiro.46x@st.kyoto-u.ac.jp

**Yuki Imanishi**
Department of Mechanical Engineering and Science
Kyoto University
Kyoto daigaku-katsura 4, Nishikyo-ku, Kyoto 615-8540, Japan
imanishi.yuki.23m@st.kyoto-u.ac.jp

**Hideshi Hanazaki**
Department of Mechanical Engineering and Science
Kyoto University
Kyoto daigaku-katsura 4, Nishikyo-ku, Kyoto 615-8540, Japan
hanazaki.hideshi.5w@kyoto-u.ac.jp

## ABSTRACT

The density and velocity fields of grid-generated turbulence in a salt-stratified fluid are measured by the laser-induced fluorescence (LIF) and the particle image velocimetry (PIV) for several different mesh Froude numbers. The potential-energy spectrum shows a local reduction near the primitive wavenumber of stratified fluid $k_P = \sqrt{N/\nu}$ ($N$ is the Brunt-Väisälä frequency, and $\nu$ is the kinematic viscosity of fluid), which strongly supports the recent results from direct numerical simulations by Okino & Hanazaki (2020). The examination of the Froude number dependence suggests that for very strong density stratification, density perturbations below the primitive scale are hardly generated, even for high Schmidt numbers.

## INTRODUCTION

The atmosphere and the ocean, when averaged in time, are the density stratified fluids with larger density at lower altitude, and their dynamics are greatly influenced by the density stratification. For example, the meridional circulation of the deep ocean is driven by the density difference of seawater, whose density is determined by temperature and salinity.

The salinity, in particular, has a very small molecular diffusivity, so that the Schmidt number $Sc(=\nu/\kappa)$ is as large as 700 ($\nu$ is the kinematic viscosity of fluid and $\kappa$ is the diffusion coefficient). According to a theory established by Batchelor (1959), a high-$Sc(\gg 1)$ scalar in turbulence diffuses at the Batchelor wavenumber $k_B = Sc^{1/2}k_K$ ($k_K$ is the Kolmogorov wavenumber) if the scalar does not change the density of the fluid and can be assumed to be passive.

Most of the experiments on density stratified turbulence have been used saltwater, with which the density stratification can be easily generated (e.g. Stillinger et al. 1983; Itsweire et al. 1986; Fincham et al. 1996; Praud et al. 2005). Density fluctuations in grid-generated stratified turbulence were measured by a conductivity probe in a series of water-channel experiments by Stillinger et al. (1983) and Itsweire et al. (1986), but the spatial resolution of the probe was not high enough to resolve scales smaller than the Kolmogorov scale.

Recently, direct numerical simulations of decaying stratified turbulence of high Schmidt numbers have been performed to reveal the behaviour of small-scale density fluctuations below the Kolmogorov scale (Okino & Hanazaki 2019, 2020). In particular, Okino & Hanazaki (2020) studied the case of $Sc = 700$ (corresponding to saltwater) and showed that the power spectrum of potential energy (or density variance) decreases locally at the primitive wavenumber of stratified tur-

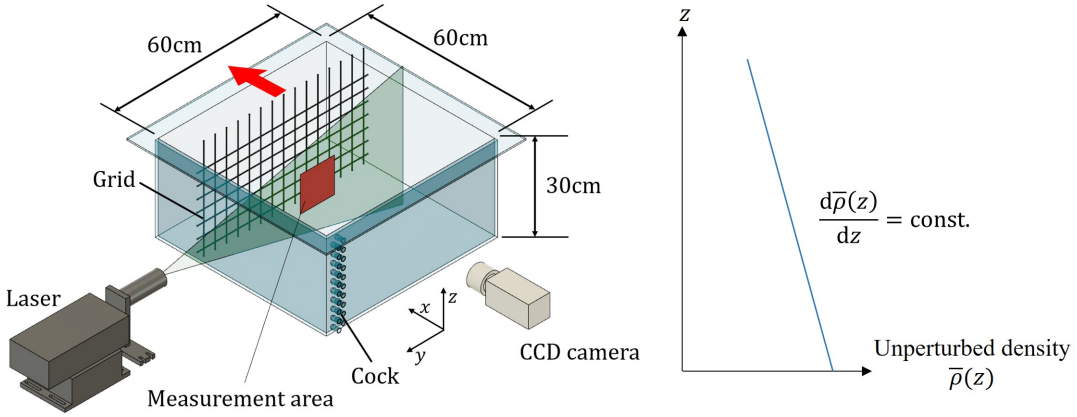


Figure 1. Schematic of the experimental facilities. A uniform density stratification is initially generated in the test tank.

bulence $k_P = \sqrt{N/\nu}$ ($N$ is the Brunt-Väisälä frequency) after the initial turbulence decays so much that the buoyancy effect reaches the Kolmogorov scale. The local reduction of the potential energy spectrum was found to be caused by the persistently counter-gradient vertical density flux at small scales (cf. Hanazaki & Hunt 1996; Komori & Nagata 1996).

In the present study, we have measured the density (or salinity) field of grid-generated turbulence in a salt-stratified fluid by the laser induced fluorescence (LIF) with a spatial resolution high enough to resolve sub-Kolmogorov scales, with the aim of validating the numerical prediction (Okino & Hanazaki 2020) and investigating the Froude number dependence of the small-scale density fluctuations.

## METHODS

In the present experiments, we excited turbulence by moving a square grid horizontally in a salt-stratified fluid generated in a test tank, and measured the density and velocity fields in their decaying process. The test tank with a square bottom of $60 \times 60$ cm$^2$ was filled with a linearly stratified water up to a height of 28 cm by a two-tank method (Fortuin 1960) (figure 1). The refractive index in the fluid was made constant using ethanol (index matching; cf. Daviero et al. (2001)) to improve the accuracy of the LIF measurement. The unperturbed density distribution $\overline{\rho}(z)$ ($z$ is the vertical coordinate) is obtained by sampling a small amount of fluid from cocks attached to one of the sidewalls of the test tank and measuring its density by a density meter (DMA4500M, Anton Paar) with an accuracy of $5 \times 10^{-5}$ g cm$^{-3}$. The Brunt-Väisälä frequency is determined by $N = \sqrt{(-g/\rho_0)(d\overline{\rho}(z)/dz)}$, where $\rho_0$ is the density at the bottom, and $g$ is the gravitational acceleration.

We used two grids with different mesh widths $M$ and rod diameters $d$, i.e. $(M,d) = (4.0\text{ cm}, 0.4\text{ cm})$ and $(8.0\text{ cm}, 0.8\text{ cm})$, but with the same solidity $\sigma = (d/M)(2 - d/M) = 0.19$. The square grid is moved horizontally along the rail at the top of the tank by a DC motor (BXS230A-10S, Oriental Motor) at a constant speed $U$.

The density distribution in a vertical plane is measured by LIF using a continuous-wave laser (488 nm, 4 W). The laser beam is vertically expanded into a laser sheet using a cylindrical lens. As the fluorescent dye, we used Rhodamine 110, whose peak absorption wavelength is 496 nm and whose peak fluorescence wavelength is 520 nm. The fluorescence of Rhodamine 110 was photographed by a CCD camera (Hisense 4MC, Dantec Dynamics; C9300-024, Hamamatsu Photonics; 12 bits, 11 Hz) equipped with a band-pass filter with a transmission wavelength of $534.5 \pm 21.5$ nm. A lens with a focal length of 50 mm (Nikkor 50mm f/1.2, Nikon) is used to observe the area of $18 \times 18$ cm$^2$ at the centre of the cross-section of the test tank.

Since the dye concentration is made to be proportional to the salinity (and the density) in the initial quiescent fluid, the density remains generally proportional to the dye concentration even after turbulence is excited by the grid. Using the principle that the intensity of the fluorescence increases with the concentration of the fluorescent dye (the Beer-Lambert law), the local density of the fluid can be determined by the light intensity photographed by the CCD camera. We should note that the proportionality between the density and the dye concentration is incomplete below their diffusive scale due to the difference in the Schmidt numbers of the fluorescent dye ($Sc \sim 2100$–$3500$) and saltwater ($Sc \sim 700$). However, we will restrict our focus to scales several times smaller than the Kolmogorov scale, and will not discuss scales as small as the Batchelor scale.

The velocity field is measured by the particle image velocimetry (PIV) using a double-pulsed Nd:YAG laser (Dual Power 65-15, Dantec Dynamics; Nano S PIV, Litron Lasers; 532 nm, 65 mJ, 15 Hz) and an acrylic emulsion as the seeding particles.

The values of the mesh Reynolds number $Re_M = UM/\nu$ and the mesh Froude number $Fr_M = U/(NM)$ used for the present experiments are listed in table 1.

The horizontal Reynolds number and the horizontal Froude number are defined by $Re_h = v_{\rm rms}^4/(\nu\varepsilon)$ and $Fr_h = \varepsilon/(Nv_{\rm rms}^2)$, respectively, where $v_{\rm rms}$ is the root-mean-square (r.m.s) horizontal velocity and $\varepsilon$ is the kinetic energy dissipation rate. The buoyancy Reynolds number defined by $Re_b = \varepsilon/(\nu N^2)$ is a measure of stratification effects at small scales and is related to the horizontal Reynolds and Froude numbers by $Re_b = Re_h Fr_h^2$. These non-dimensional numbers at the time when the kinetic energy dissipation rate becomes maximum are also given in table 1. The initial Froude numbers in the present experiments are smaller than those of Itsweire et al. (1986) ($Fr_h > 2$) though the initial Reynolds numbers are similar ($Re_h \sim 200$). The initial buoyancy Reynolds number is sufficiently larger than unity, so that small-scale fluctuations would not initially be affected by buoyancy, unlike the experiments by Praud et al. (2005).

The following two non-dimensional times are used to describe the results. One is the advection time $t_L = Ut/M$ and the other is the buoyancy time $t_N = t/T_{BV} = Nt/(2\pi)$, where $T_{BV}$ is the Brunt-Väisälä period. The ratio of the two is determined

Table 1. List of the parameter used for the experiments. The values at the time when the kinetic energy dissipation rate becomes maximum are denoted by the subscript 0.

| $Fr_M$ | $Re_M$ | $M$ (cm) | $U$ (cm s$^{-1}$) | $N$ (s$^{-1}$) | $\varepsilon_0$ (cm$^2$ s$^{-3}$) | $v_{\mathrm{rms},0}$ (cm s$^{-1}$) | $Re_{h,0}$ | $Fr_{h,0}$ | $Re_{b,0}$ |
|---|---|---|---|---|---|---|---|---|---|
| 16 | 9200 | 4.0 | 23.0 | 0.37 | 1.07 | 1.33 | 290 | 1.6 | 780 |
| 7.0 | 9200 | 4.0 | 23.0 | 0.83 | 0.978 | 1.28 | 270 | 0.72 | 140 |
| 1.8 | 9200 | 8.0 | 11.5 | 0.83 | 0.633 | 1.12 | 250 | 0.61 | 92 |

by the mesh Froude number, i.e.

$$\frac{t_L}{t_N} = 2\pi Fr_M. \tag{1}$$

## RESULTS

We first show in figure 2 the temporal variation of the distribution of potential energy, $(g^2/2\rho_0^2N^2)\rho'^2$, and kinetic energy, $(1/2)(v^2+w^2)$, in a vertical plane for $Fr_M = 16$, where $\rho'$ is the density perturbation, $v$ the horizontal velocity and $w$ the vertical velocity. At an early time of $t_L = 29.3$, thin sheet-like structures of high potential energy are distributed isotropically without a specific direction (figure 2a), since the buoyancy time is smaller than unity ($t_N = t_L/(2\pi Fr_M) \sim 0.3$) and the buoyancy effect has not been significant at small scales. Then, the distribution of kinetic energy is also isotropic (figure 2b). The smallest scale of potential energy is much smaller than that of kinetic energy because the Schmidt number is much larger than unity ($Sc \sim 700$ for saltwater). Figures 2(c,d) show that similar structures can be seen even at a later time of $t_L = 78.8$ when the buoyancy time is still less than unity ($t_N \sim 0.8$). We note that the thin sheet-like structures of high-Schmidt number scalar is observed also in isotropic turbulence with a constant concentration-gradient of a passive (i.e. non-buoyant) scalar (Brethouwer et al. 2003).

After the buoyancy time exceeds unity (figure 2e when $t_N \sim 1.8$), the distribution of the potential energy becomes anisotropic in that the fine structures of high potential energy cluster together to form a horizontally long structure (whose length is $\sim M$). The kinetic energy distribution also has such horizontal structures (figure 2f) though the structures as fine as those seen in the potential energy distribution does not exist.

As time passes further ($t_N \sim 3.0$), small-scale structures of potential energy have largely decayed, but large-scale clouds composed of small-scale streaks can be identified (figure 2g). The horizontal and vertical scales of the cloud are comparable to those of high kinetic energy (figure 2h). The temporal variation of the structure of the potential energy distribution from thin sheets to clouds is consistent with the recent result of direct numerical simulation at $Sc = 700$ (Okino & Hanazaki 2020).

We next compare the potential energy distributions for three mesh Froude numbers ($Fr_M = 16, 7.0$ and $1.8$) at a fixed advection time $t_L(\sim 30)$. It should be noted here that the buoyancy times $t_N(= t_L/(2\pi Fr_M))$ are different for different mesh Froude numbers. As mentioned earlier, the potential energy distribution for $Fr_M = 16$ (figure 2a) is isotropic and does not significantly affected by buoyancy since the buoyancy time is $t_N \sim 0.3(\ll 1)$. Similarly, for $Fr_M = 7.0$ (figure 3a), the buoyancy time is still less than unity ($t_N \sim 0.8$), so that the sheet-like structures of the potential energy are distributed almost isotropically. However, for the smallest mesh Froude number of $Fr_M = 1.8$ (figure 3b), the buoyancy time becomes so large ($t_N \sim 3.0$) that the potential energy distribution exhibits horizontal cloud structures, resembling those observed for $Fr_M = 16$ at the same buoyancy time (figure 2g). This suggests that the pattern of the potential energy distribution is better determined by the buoyancy time rather than the advection time.

Figure 4 shows the temporal variation of the vertical spectrum of potential energy,

$$E_P(k_z) = \frac{g^2}{2\rho_0{}^2N^2}\sum_{k_y}\left(\left|\widehat{\rho'}(k_y,k_z)\right|^2 + \left|\widehat{\rho'}(k_y,-k_z)\right|^2\right)\frac{1}{k_{\min}}, \tag{2}$$

where $\widehat{\rho'}(k_y,k_z)$ is the two-dimensional Fourier component of the density perturbation $\rho'(y,z)$ with a two-dimensional wave-vector $(k_y,k_z)$. In decaying stratified turbulence, the Kolmogorov wavenumber $k_K$ decreases with time, while the Ozmidov wavenumber $k_O$ increases, since the kinetic energy dissipation rate decreases. In the present experiments, $k_K$ and $k_O$ coincide at a buoyancy time of $t_N \sim 1$.

When $Fr_M = 16$ (figure 4a), the potential energy spectrum exhibits Batchelor's $k^{-1}$ law near the Kolmogorov wavenumber at $t_N = 0.6$. As time passes, however, $E_P(k_z)$ decreases locally and bends at the primitive wavenumber of stratified fluid $k_P = \sqrt{N/\nu}$, in agreement with the result of DNS (Okino & Hanazaki, 2020). The local reduction of the potential energy at the primitive wavenumber is observed also for the stronger stratification of $Fr_M = 7.0$ and $1.8$ (figure 4b,c) though the bending at $k_z = k_P$ is less conspicuous.

The temporal variation of the amount of the potential energy at each wavenumber can be seen more readily from the pre-multiplied spectrum (figure 5), where the area below the spectral curve corresponds to the amount of energy. Initially ($t_N \simeq 0.6$), the pre-multiplied spectrum for $Fr_M = 16$ (figure 5a) has a plateau ($k_zE_P(k_z) \simeq$ const.) near the Kolmogorov wavenumber, which corresponds to the $k^{-1}$ law observed in figure 4(a). When $k_K$ and $k_O$ approaches ($t_N \simeq 1.0$), the potential energy decrease locally at $k_z = k_P$, generating two peaks in the pre-multiplied spectrum ($k_zM \sim 10$ and $10^2$).

Similarly for stronger stratification ($Fr_M = 7.0$ and $1.8$), we can identify the local reduction of the potential energy at the primitive wavenumber and the resulting two potential-energy peaks (figure 5b,c). It should be noted, however, that the energy below $k_P$ increases relative to the energy above $k_P$ as the stratification increases. In other words, for weak stratification of $Fr_M = 16$ (figure 5a), the potential energy is contained more at small scales ($k_z > k_P$) than large scales ($k_z < k_P$), whereas for strong stratification of $Fr_M = 1.8$ (figure 5c), the energy is contained more at large scales ($k_z < k_P$). The relative increase in the potential energy at large scales would be because the potential energy is persistently converted into the kinetic energy at the primitive wavenumber (Okino &

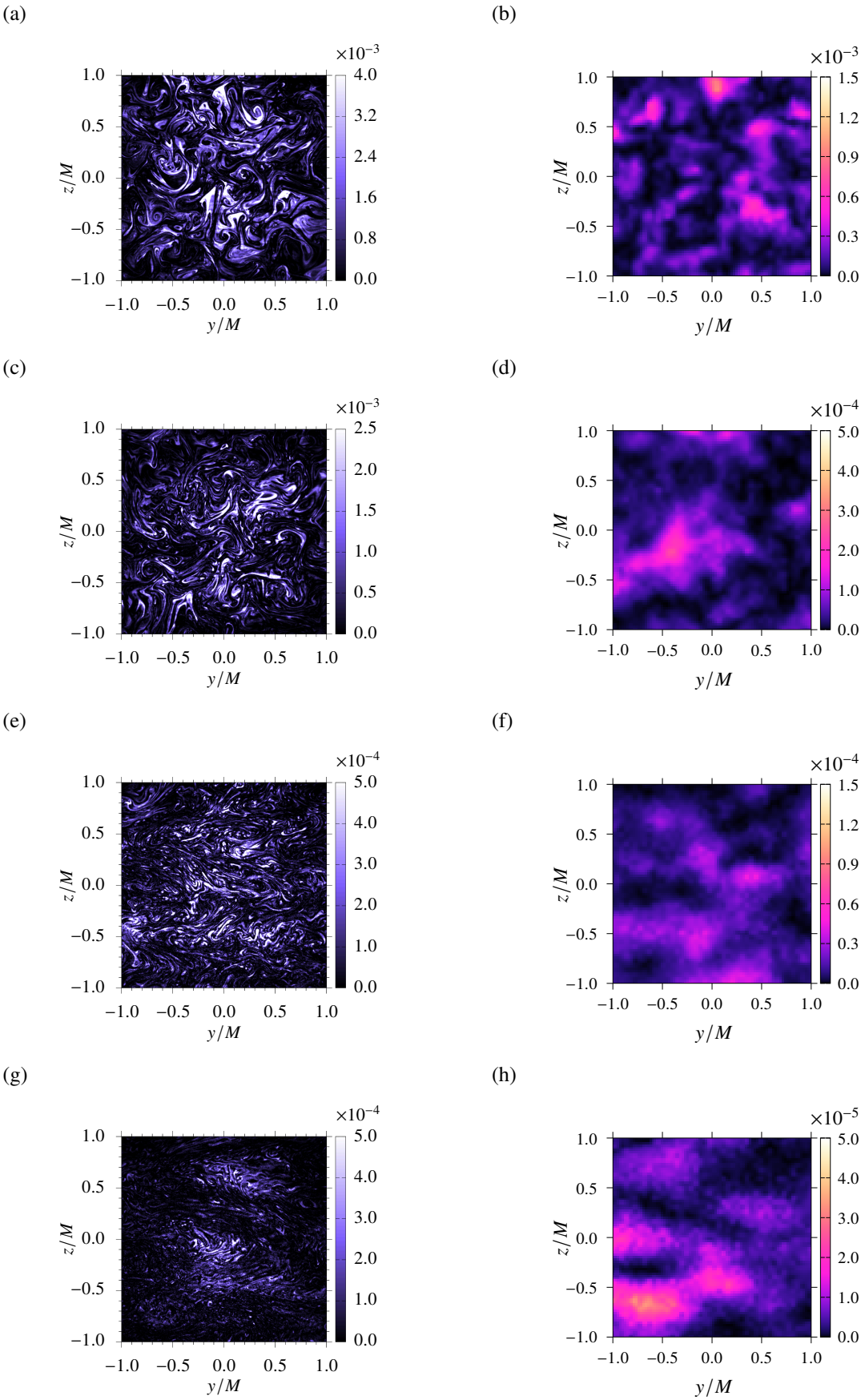


Figure 2. Temporal evolution of the distribution of (a,c,e,g) potential energy $(g^2/2\rho_0^2 N^2)\rho'^2/U^2$ and (b,d,f,h) kinetic energy $(1/2)(v^2+w^2)/U^2$ in the vertical plane for $Fr_M = 16$. (a,b) $t_N = 0.3, t_L = 29.3$, (c,d) $t_N = 0.8, t_L = 78.8$, (e,f) $t_N = 1.8, t_L = 173.1$, and (g,h) $t_N = 3.0, t_L = 288.1$.

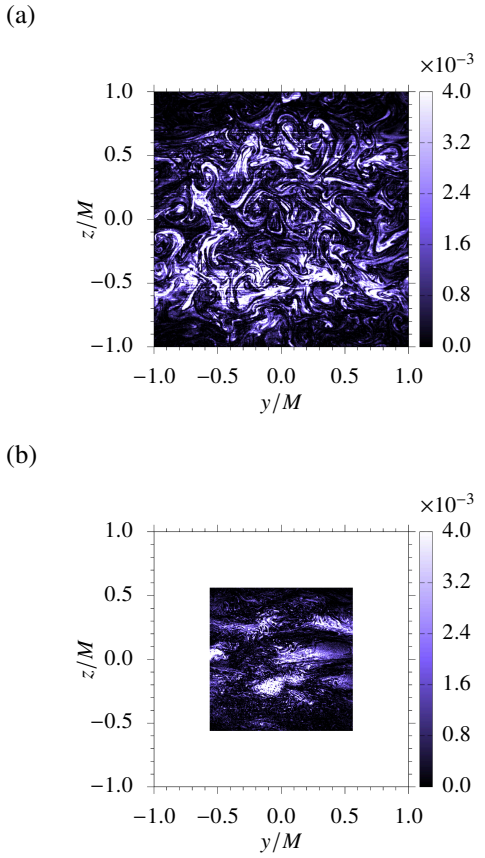


Figure 3. Froude number dependence of the potential energy distribution $(g^2/2\rho_0^2N^2)\rho'^2/U^2$ in the vertical plane at $t_L \sim 30$. (a) $Fr_M = 7.0, t_N = 0.8, t_L = 36.2$, and (b) $Fr_M = 1.8, t_N = 3.0, t_L = 33.2$.

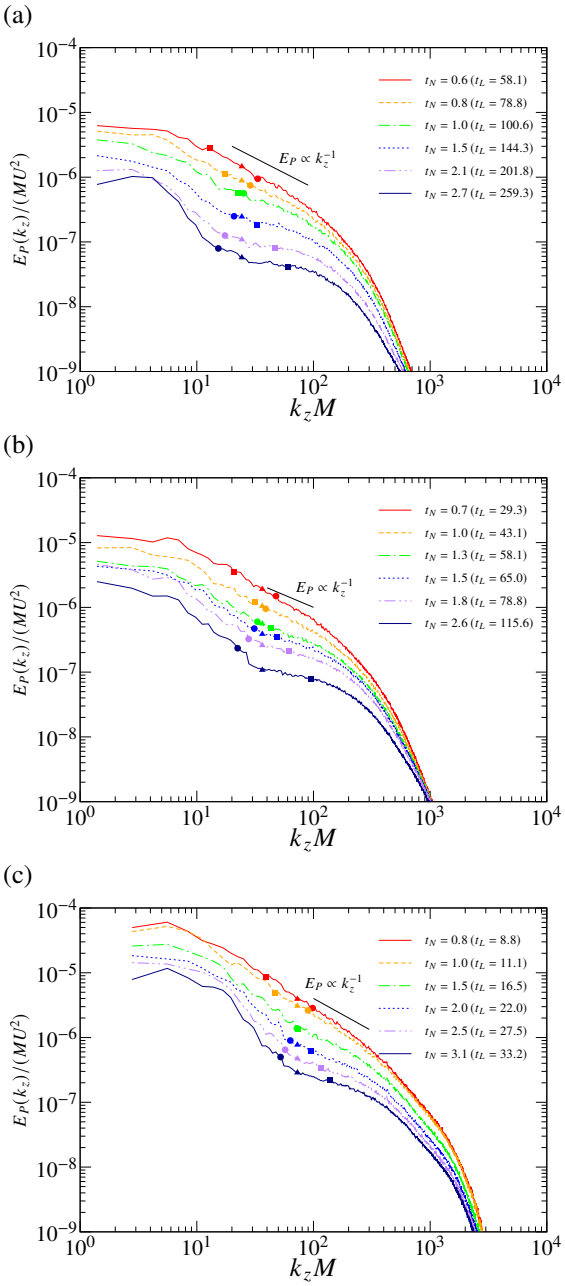


Figure 4. The temporal evolution of the vertical spectrum of potential energy $E_P(k_z)$ for (a) $Fr_M = 16$, (b) $Fr_M = 7.0$, and (c) $Fr_M = 1.8$. Symbols on each spectral curve show the Kolmogorov wavenumber $k_K$ (circle), the Ozmidov wavenumber $k_O$ (square) and the primitive wavenumber of stratified fluid $k_P$ (triangle), which are defined by $k_K = (\varepsilon/\nu^3)^{1/4}$, $k_O = (N^3/\varepsilon)^{1/2}$ and $k_P = (N/\nu)^{1/2}$, respectively.

Hanazaki 2020) earlier than it is transferred to high wavenumbers.

As the stratification becomes further stronger, the potential energy is expected to be absent at wavenumbers larger than the primitive wavenumber, even at high Schmidt numbers. To confirm this conjecture, we have performed a direct numerical simulation at the initial Froude number of $Fr_0 = U_0/(NL_0) = 0.1$ and $Sc = 700$, where $L_0$ is the initial integral length and $U_0$ the initial r.m.s. velocity. This initial Froude number is several times smaller than the horizontal Froude number in the present experiments ($Fr_h > 0.6$; cf. table 1). The numerical methods are same as Okino & Hanazaki (2020).

Figure 6 shows the temporal evolution of the pre-multiplied potential-energy spectrum at $Fr_0 = 0.1$. Indeed, the potential energy is not transferred to wavenumbers above the primitive wavenumber (indicated by the vertical dotted line) at all, and the most of the energy remains at the initial integral scale ($kL_0 \sim 3$).

## CONCLUSIONS

We have performed tank experiments using a salt-stratified water to investigate the time evolution and the Froude number dependence of the density field of grid-generated turbulence. The distributions of the density and velocity in a vertical plane are measured by LIF and PIV, respectively.

Initially when the buoyancy effect has not reached wavenumbers higher than the Kolmogorov wavenumber, the spectrum of potential energy exhibits the $k^{-1}$ law near the Kolmogorov wavenumber. As time elapses and the buoyancy effect extends beyond the Kolmogorov wavenumber, the potential-energy spectrum shows a local reduction near the primitive wavenumber of stratified fluid, which is in good agreement with the recent result from a direct numerical simulation by Okino & Hanazaki (2020).

When the density stratification is very strong, density perturbations below the primitive scale are hardly generated, even for high Schmidt numbers such as saltwater. This would be because the potential energy is persistently converted into the kinetic energy at the primitive wavenumber earlier than it is

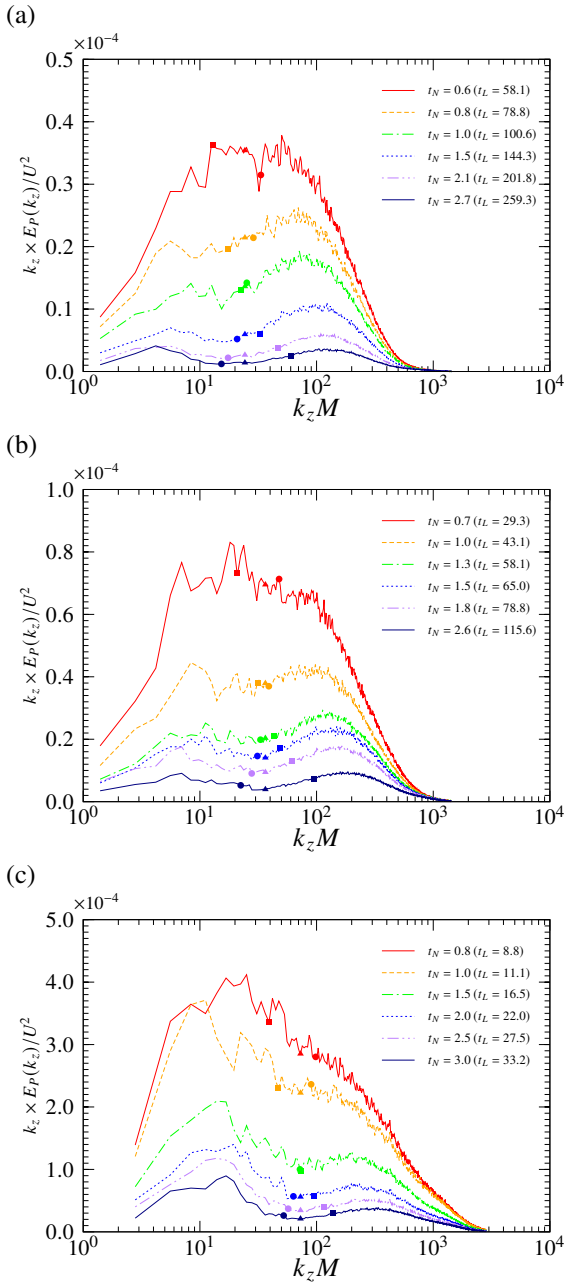


Figure 5. The temporal evolution of the vertical spectrum of potential energy in the pre-multiplied form, i.e. $k_z \times E_P(k_z)$, for (a) $Fr_M = 16$, (b) $Fr_M = 7.0$, and (c) $Fr_M = 1.8$. Symbols on each spectral curve show the Kolmogorov wavenumber $k_K$ (circle), the Ozmidov wavenumber $k_O$ (square) and the primitive wavenumber of stratified fluid $k_P$ (triangle).

transferred to high wavenumbers.

This study was supported by JSPS KAKENHI grant nos 21H01247, 21K03875, and used computational resources provided by Tohoku University through the HPCI System Research Project (hp210042) and by the Earth Simulator Center of JAMSTEC.

## REFERENCES

Batchelor, G. K. 1959 Small-scale variation of convected quantities like temperature in turbulent fluid. Part 1. General discussion and the case of small conductivity. *J. Fluid Mech.* **5**, 113–133.

Brethouwer, G., Hunt, J. C. R. & Nieuwstadt, F. T. M. 2003 Micro-structure and Lagrangian statistics of the scalar field with a mean gradient in isotropic turbulence. *J. Fluid Mech.* **474**, 193–225.

Daviero, G. J., Roberts, P. J. W. & Maile, K. 2001 Refractive index matching in large-scale stratified experiments. *Exp. Fluids* **31**, 119–126.

Fincham, A. M., Maxworthy, T. & Spedding, G. R. 1996 Energy dissipation and vortex structure in freely decaying stratified grid turbulence. *Dynam. Atmos. Oceans* **23**, 155–169.

Fortuin, J. M. H. 1960 Theory and application of two supplementary methods of constructing density gradient columns. *J. Polym. Sci.* **44**, 505–515.

Hanazaki, H. & Hunt, J. C. R. 1996 Linear processes in unsteady stable stratified turbulence. *J. Fluid Mech.* **318**, 303–337.

Itsweire, E. C., Helland, K. N. & Van Atta, C. W. 1986 The evolution of grid-generated turbulence in a stably stratified fluid. *J. Fluid Mech.* **162**, 299–338.

Komori, S. & Nagata, K. 1996 Effects of molecular diffusivities on counter-gradient scalar and momentum transfer in strongly stable stratification. *J. Fluid Mech.* **326**, 205–237.

Okino, S. & Hanazaki, H. 2019 Decaying turbulence in a stratified fluid of high Prandtl number. *J. Fluid Mech.* **874**, 821–855.

Okino, S. & Hanazaki, H. 2020 Direct numerical simulation of turbulence in a salt-stratified fluid. *J. Fluid Mech.* **891**, A19.

Praud, O., Fincham, A. M. & Sommeria, J. 2005 Decaying grid turbulence in a strongly stratified fluid. *J. Fluid Mech.* **522**, 1–33.

Stillinger, D. C., Helland, K. N. & Van Atta, C. W. 1983 Experiments on the transition of homogeneous turbulence to internal waves in a stratified fluid. *J. Fluid Mech.* **131**, 91–122.

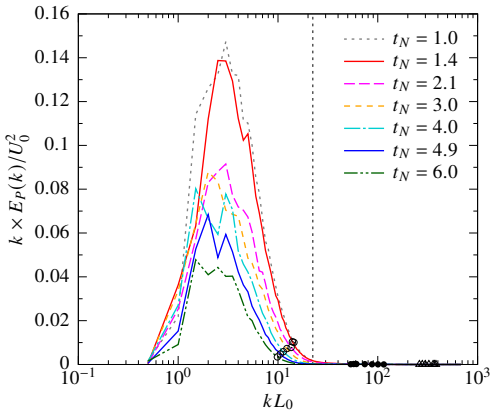


Figure 6. Numerical result of the radial spectrum of potential energy in the pre-multiplied form, i.e. $k \times E_P(k)$, for very strong stratification. The initial Froude and Reynolds numbers are $Fr_0 = U_0/(NL_0) = 0.1$ and $Re_0 = U_0 L_0/\nu = 50$, respectively. Symbols on each spectral curve show the Kolmogorov wavenumber $k_K$ (open circle), the Ozmidov wavenumber $k_O$ (closed circle) and the Batchelor wavenumber $k_B$ (triangle). The vertical dotted line indicates the primitive wavenumber of stratified fluid $k_P$.